Construction and characterization of visible light active Pd nano-crystallite decorated and C-N-S-co-doped TiO₂ nanosheet array photoelectrode for enhanced photocatalytic degradation of acetylsalicylic acid

Dong Li[a], Jialin Jia[a], Tong Zheng[c], Xiuwen Cheng[d], Xiujuan Yu[a,b,*]

[a] Department of Environmental Science and Engineering, Heilongjiang University, Xuefu Road 74, Nangang District, Harbin 150080, Heilongjiang Province, PR China
[b] Key Laboratory of Chemical Engineering Process & Technology for High-efficiency Conversion, Harbin, College of Heilongjiang Province, PR China
[c] School of Municipal and Environmental Engineering, Harbin Institute of Technology, Huanghe Road 73, Nangang District, Harbin 150090, PR China
[d] Key Laboratory for Environmental Pollution Prediction and Control, Gansu Province, College of Earth and Environmental Sciences, Lanzhou University, Lanzhou 730000, PR China

ARTICLE INFO

ABSTRACT

A photo-assisted deposition technique was adopted to construct highly dispersed Pd nano-crystallites on C-N-S-co-doped TiO₂ nanosheets (Pd/C-N-S-TiO₂ NS) arrays photoelectrodes prepared by one-step hydrothermal synthesis. The morphology, elemental composition, crystal structure, light absorption capability and photoelectrochemical (PECH) property of as-obtained Pd/C-N-S-TiO₂ NS electrodes were determined and investigated through the various characterizations. The photocatalytic (PC) and photo-electrocatalytic (PEC) activity of the Pd/C-N-S-TiO₂ NS electrode was evaluated through the degradation of acetylsalicylic acid and the formation of •OH radicals. Compared with pristine TiO₂ NS, Pd/TiO₂ NS and C-N-S-TiO₂ NS, Pd/C-N-S-TiO₂ NS electrode displayed greatly enhanced PC and PEC activity towards the degradation of acetylsalicylic acid under visible light ($\lambda > 420$ nm) or Xenon light irradiation. The synergy effect of interfacial transfer of photoinduced electrons between Pd nanoparticles and TiO₂ NS as well as the external potential and intense visible light absorption induced by C, N and S co-doing promoted the effective charge separation and transfer and more visible photons to participate in the catalytic process on obtained Pd/C-N-S-TiO₂ NS, which were evidenced by a series of characterizations, resulting in highly efficient and stable PC and PEC activity. Moreover, the probable visible light PEC mechanism was proposed.

© 2016 Elsevier B.V. All rights reserved.

1. Introduction

Photocatalytic (PC) oxidation has been recognized as one of the most promising techniques for removal of environment pollutants [1–3]. Over the past decades, owing to its environmental friendliness, superior PC capacity, high chemical stability and cheapness, titanium dioxide (TiO₂) semiconductor has been considered as a remarkable photocatalyst [4]. Nevertheless, the practical applications of TiO₂ nano-materials were greatly restrained by its intrinsic defects. Firstly, the wide band gap energy of pure TiO₂ (3.0–3.2 eV)

restricts its PC application in the ultraviolet (UV) region, which merely accounts for approximately 4% of the sunlight energy [5]. Secondly, the rapid recombination of photogenerated electrons and holes (e^-/h^+) pairs after excitation may result in the low quantum efficiency, and then lowering the PC activity during the degradation of contaminants [5]. Thirdly, the pulverous TiO₂ nano-catalyst is very difficult to separate and recycle from the slurry system, thereby leading to the knotty issue of secondary pollution and reuse of catalyst. Hence, masses of works have been carried out to enhance the visible light PC activity and lifecycle of TiO₂ nano-catalyst [6].

Since the pioneering discovery of N-doped TiO₂ by Asahi et al. [7], numerous endeavors on non-metal element, such as C, N, S, B and F, doping have been carried out to utilize effectively visible light of solar spectrum, and enhance the PC performance of TiO₂ nano-

materials [8–12]. Among these dopants, Nitrogen-doped TiO_2 has been attracted considerable attentions because nitrogen has a similar atomic size to oxygen, low ionization energy and metastable center formation as well as stability [8]. Doping TiO_2 with nitrogen can induce band gap narrowing through embedding nitrogen atom into the lattice of TiO_2, which can create the overlap of oxygen 2p states and nitrogen 2p states just on the top of the valence band of TiO_2 at substitutional lattice sites or the inter-gap states, therefore enhancing the light absorption capacity in visible range, resulting in an improved visible light PC performance [13]. In the case of carbon doping, carbon atoms is usually demonstrated infiltrating to the lattice of TiO_2 replacing either lattice Ti atom and generate carbonate species (C—O and C=O) or lattice O atom and produce Ti–C bond, which forms a hybrid orbit under the conduction band or above the valence band of TiO_2, respectively, so bestows an increased visible light absorption [9]. For sulfur impurity, sulfur atom can substitute either the titanium as a cation or the oxygen as an anion, which depended closely on the synthesis routes and sulfur sources. Sulfur-doping also induces the band gap energy decrease and promotes the visible light PC activity [10]. Afterwards, researchers have been devoted to exploit doping TiO_2 with two or three kinds of nonmetal elements simultaneously to arouse a higher visible light PC activity than single element doping due to the merits benefited from each dopant [14,15]. Trevisan et al. [16] have confirmed that the multi-elements co-doping of C and N is greatly better than single N doping in improving the photocatalytic activity of TiO_2. To tackle the problem of low quantum efficiency, the precious metals nano-crystallites have attracted extensive interest as one of versatile candidates employed in PC and PEC processes recently [17,18]. Particularly, precious metal palladium (Pd) immobilized on the supports displayed extraordinary properties in the electro-catalytic (EC) and PC reactions [18,19]. Hence, rational design and effective preparation of TiO_2-based nano-materials have attracted widely attentions.

As demonstrated later, the quantum efficiency and light absorption of photocatalysts greatly depend on its micromorphology [20], thus, many efforts have been focus on devising novel highly ordered TiO_2-based nano-architectures materials, including nanosheets [21], nanowires [22], nanorods [23], nanobelts [24] and nanotubes [25] direct growth onto the titanium substrates by anodization or hydrothermal method. These TiO_2-based nano-materials can display prominent PC activity for removal of hazardous pollutants and H_2 production or photo-electricity conversion efficiency on solar cell due to exceptional microstructure for faster electron transportation and intense light harvesting performance [21–25]. Moreover, the TiO_2 nano-catalysts in-situ grew on the titanium substrates exhibit an advantage over the deficiency encountered with pulverous TiO_2 suspensions [26]. Afterwards, a great deal of studies has been performed. More recently, Wang et al. [21] indicated that TiO_2 nanosheets film exhibits higher PC activity than TiO_2 nanotubes. Furthermore, our group had fabricated TiO_2 nanosheets (NSs) through a simple hydrothermal synthesis [27,28], which displayed convenient transfer of photoinduced charge carriers. The study results revealed that the prepared TiO_2 NSs can prominently improve the PEC activity compared to TiO_2 nanobelts and TiO_2 nanowires which were widely investigated in previous researches [27]. Although there were many literatures reported about the synthesis of TiO_2 nanosheets nano-photocatalysts. But, these literatures were mainly related to the pulverous TiO_2 nanoheets [29–31]. And, to the best of our knowledge, the precious metal and multi-nonmetal modified simultaneously TiO_2 nanosheets immobilized on the Ti plate have not been construction and investigated by others yet.

Herein, in the present paper, we report a novel visible light active Pd nano-crystalline decorated and C-N-S-co-doped TiO_2 hybrid nanosheet (Pd/C-N-S-TiO_2 NS) array photoelectrode prepared by a two-step approach for the first time, *i.e.*, the one-step hydrothermal technique followed by photo-assisted deposition strategy. The morphology, surface composition, structure and optical properties as well as PECH performances of as-prepared Pd/C-N-S-TiO_2 NS photoelectrode were widely characterized and investigated. Furthermore, the PC and PEC activities of as-prepared Pd/C-N-S-TiO_2 NS photoelectrode were evaluated by the degradation of acetylsalicylic acid and formation of the •OH radicals. It is demonstrated that the advantages of combining TiO_2 NS with non-mental C, N and S and metallic Pd nanoparticles are that they help absorb visible photons and transfer the photogenerated electrons more efficiently. Compared with as-prepared TiO_2 NS, Pd/TiO_2 NS and C-N-S-TiO_2 NS, the much enhancing effect of the Pd/C-N-S-TiO_2 NS photoelectrode on the PC and PEC activities was observed under visible light or Xenon lamp irradiation, and the interrelations between the structure and the performance were discussed in details according to the results of a systematic characterization. Finally, the enhanced visible light PC mechanism and photostability of the as-prepared Pd/C-N-S-TiO_2 NS photoelectrode were proposed and investigated, respectively.

2. Experimental

2.1. Materials

Ti foils (0.5 mm thickness, 99.8% purity) were purchased from Dongguan Fu Tai Metal Materials Co., Ltd., China. All of the chemicals employed in our work were analytical grade and used without further purification. Deionized water was used throughout all experiments.

2.2. Preparation of Pd/C-N-S-TiO_2 NS array photoelectrode

C-N-S-TiO_2 NS array photoelectrode was fabricated through one step hydrothermal reaction of titanium foils. Prior to hydrothermal reaction, titanium foils were cleaned in an ultrasonic bath of detergent solution, acetone, ethanol and deionized water for 10 min each round in that order. Next, the as-treated titanium foils were immersed in a mixture of HF and diluted HNO_3 acids (HF: HNO_3: H_2O = 1:4:5 in volume) for 45 s. Afterwards, these titanium foils were rinsed with ethanol and deionized water for several times, respectively, and then dried at room temperature. After that, the as-rinsed titanium foils were placed against the wall of a 50 mL *para*-polyphenyl-lined stainless steel autoclave filled with 20 mL aqueous solution containing 1 mol L^{-1} NaOH and 0.1 mol L^{-1} cystine. Then, the sealed autoclave was maintained in an electric oven at 170 °C for 28 h, followed by naturally cooling down to room temperature. After hydrothermal procedure, titanium foils covered with nanosheet array were rinsed by deionized water for several times and immersed in 1 M HCl solution for 24 h aimed at replacing Na$^+$ with H$^+$, and dried in ambient condition. Finally, the obtained samples were calcinated at 500 °C in a muffle furnace for 2 h with heating and cooling rates of 3 °C min^{-1}.

Pd nano-crystallite was deposited onto the surface of C-N-S-TiO_2 NS electrode through reducing the Pd^{2+} ions photocatalytically using PdCl$_2$ as a Pd precursor. The C-N-S-TiO_2 NS electrode was soaked into 1 mmol PdCl$_2$ solution under stirring for 0.5 h in dark so that the electrode could adequately contact and adsorb Pd^{2+}. Subsequently the electrode was exposed to 350 W Xenon light irradiation with an intensity of 29.8 KLux. When the Xenon light irradiated the C-N-S-TiO_2 NS photoelectrode, electrons could be easily excited and transferred to the surface of NS. After then, the excited electrons could promptly react with the absorbed Pd^{2+}, generating the Pd° in the form of nanoparticles. The illumination time was 1 h, sufficient to induce PC reduction of Pd^{2+} to Pd° nanoparticles on the surface of

NS. Eventually, the obtained Pd/C-N-S-TiO$_2$ NS photoelectrode was rinsed with deionized water, and dried at a temperature of 80 °C for 2 h in a vacuum oven. TiO$_2$ NS electrode was prepared without cystine and PdCl$_2$, and Pd/TiO$_2$ NS was synthesized in the absence of cystine.

2.3. Characterization

Scanning electron microscopy (SEM) images and energy dispersive X-ray spectroscopy (EDX) were measured on a field emission scanning electron microscope (FE-SEM, Hitachi S4800, Japan) with an acceleration voltage of 5 kV to record the morphology and the composition of the as-synthesized electrode. X-ray photoelectron spectroscopy (XPS, Kratos-AXIS ULTRA DLD) equipped with Al Kα X-ray source was performed to analyze the surface electronic states of the sample. All the binding energy values were calibrated using the surface adventitious carbon (C1s) at 284.6 eV as a reference. X-ray diffraction (XRD) patterns were carried out on a Bruker D8 Advance X-ray diffractometer with Cu Kα radiation (λ = 1.5418 Å) to examine the crystalline structure. The accelerating voltage and applied current were at 40 kV and 30 mA, respectively. Raman spectra were recorded at room temperature on a Jobin Yvon HR800 Raman spectrometer equipped with an Ar$^+$ ion laser at excitation wavelength of 457.9 nm. UV–vis diffuse reflection spectroscopy (UV–vis DRS) was performed on a TU-1901 spectrophotometer using BaSO$_4$ as the background over a range of 200–800 nm. Photoluminescence (PL) spectra were obtained through a FP-6500 fluorescence spectrometer (Hitachi, Japan) at room temperature. The surface photovoltage (SPV) measurements for as-prepared electrodes were performed on a home-built apparatus, which consisted of a lock in amplifier (SR830) synchronized with an optical chopper (SR540) and a double prism monochromator (SBP300). All of the SPV measurements were carried out at room temperature.

2.4. PECH measurement

PECH properties of the as-synthesized photoelectrodes were measured in a standard three-electrode configuration in homemade single-compartment quartz cell with the as-synthesized electrodes as photoanode (an active area of ca. 3 cm^2), the Pt sheet electrode as counter electrode and the saturated calomel electrode (SCE) as reference electrode. The transient photocurrent response (TPR) and open circuit potential (OCP) were measured on a LK3200 electrochemical station. Electrochemical impedance spectroscopy (EIS) curves were obtained using a computer-controlled Versa STAT 3 impedance measurement unit (Princeton Applied Research) in dark and under Xenon lamp irradiation at open circuit voltage with a frequency range from 0.01 Hz to 1 MHz. The electrolyte was 0.1 mol L^{-1} Na$_2$SO$_4$ solution. Mott-Schottky plots were performed on a CHI700e electrochemical analyzer under irradiation of Xenon lamp. The applied potential ranged from −0.8 to 0.6 V (vs. SCE) at a fixed frequency of 1 kHz with potential steps of 5 mV to determine the flat-band potential and charge carrier density. In this study, a 350 W Xenon lamp was used as the simulated sunlight illuminant to provide an illumination intensity of 29.8 KLux.

2.5. PC and PEC activities

The PC and PEC activities of the as-prepared Pd/C-N-S-TiO$_2$ NS photoelectrode were evaluated through the degradation of acetylsalicylic acid. The reaction setup diagram for photocatalysis and photoelectrocatalysis are displayed in Fig. S1 (Supplementary information). The PC degradation was carried out in a 50 mL homemade cylindrical quartz photo-reactor. A 350 W Xenon lamp was used as simulated solar light source to provide an irradiation intensity of 29.8 KLux. And the 350 W Xenon light with an ultra-violet filter (λ > 420 nm) was employed as the visible light source and placed 15 cm away from the photo-reactor. Prior to irradiation, 1 × 3 cm^2 photoreaction areas of electrode were kept into 30 mL of acetylsalicylic acid aqueous solution with a concentration of 10 mg L^{-1}. Additionally, a hose was fixed at the bottom of the photo-reactor to bubble O$_2$ or N$_2$ into the solution. Afterwards, the solution was allowed in the dark under stirring for 30 min to establish the equilibrium of adsorption/desorption. Next step, the reaction system was irradiated by Xenon lamp. At given time intervals, the collected acetylsalicylic acid were filtrated (0.45 μm) and immediately measured employing Shimadzu LC10A high performance liquid chromatography (HPLC) with a Kromasil KR100-5 C18 column (20 mm × 4.6 mm i.d.). The mobile phase was a mixture of 35% methanol and 65% MilliQ-water (containing 1% acetic acid), and was sonicated for 5 min to remove dissolved gas. The eluent was delivered with a flow rate of 1 mL/min. The detection wavelength was 276 nm and the injection volume was 20 μL. The PEC degradation was performed under the parallel condition, while a +2.0 V external voltage was applied and controlled by a two-channel output DC power supply (DH1715A-5). In addition, 0.1 mol L^{-1} Na$_2$SO$_4$ solution was utilized as the supporting electrolyte. For comparison, the PC and PEC experiments for other TiO$_2$ NS electrodes were also performed under identical conditions. Moreover, the formation of •OH radicals was detected through the fluorescence (FL) technique using a RF-5301PC fluorescence spectrophotometer.

3. Results and discussion

3.1. Morphology, surface composition and structural characterization

The typical top-view FE-SEM images of the as-prepared pristine TiO$_2$ NS, C-N-S-TiO$_2$ NS and Pd/C-N-S-TiO$_2$ NS photoelectrodes and corresponding EDX spectroscopy are displayed in Fig. 1. As shown in Fig. 1a, well aligned and highly density nano-lamellate structure could be obviously observed for pristine TiO$_2$ NS, which possessed the nanosheet lengths and the wall thickness in the range of 500–1500 nm and 10–40 nm, respectively. Noticeably, compared with the TiO$_2$ NS, the surface morphology of the C-N-S-TiO$_2$ NS were hardly any change at all (Fig. 1b), which might be ascribed to the fact that a little amount of C, N and S were entrance into the lattice of TiO$_2$ during hydrothermal reactions. Further, after photodeposition with Pd nano-crystallites (Fig. 1c), the nano-sheet structure of C-N-S-TiO$_2$ NS could still remain its integrity without any significant morphological transformation. And it could be clearly observed that the decorated Pd nano-crystallites were uniformly attached on the surface of C-N-S-TiO$_2$ NS. A high magnification top-view SEM image of Pd/C-N-S-TiO$_2$ NS of approximate area from Fig. 1c marked in red dotted line is shown in Fig. 1d. Markedly, a number of cubical Pd nanoparticles with an average length of 60 nm and thickness of 20 nm were uniformly formed. In addition, numerous spherical or cubical Pd nanoparticles with an average diameter of 10 nm were equably covered the surface of nanosheets. Meanwhile, EDX spectroscopy (Fig. 1e) of the C-N-S-TiO$_2$ NS photoelectrode revealed the existence of C, S, Ti and O elements. Therein, C and S probably derived from the dopants during the synthetic process. On the contrary, as displayed in Fig. 1f, the Pd decorated C-N-S-TiO$_2$ NS sample not only contained C, S, Ti and O, but also exhibited the existence of Pd element, confirming that Pd nano-crystallite was successfully deposited onto the nanosheets through a light-induced chemical reduction. Interestingly, there were no signal observed relating to the presence of N element in the EDX spectrum of C-N-S-TiO$_2$ NS and Pd/C-N-S-TiO$_2$ NS, which may be attributed to the content of nitrogen element was too little to be detected by EDX.
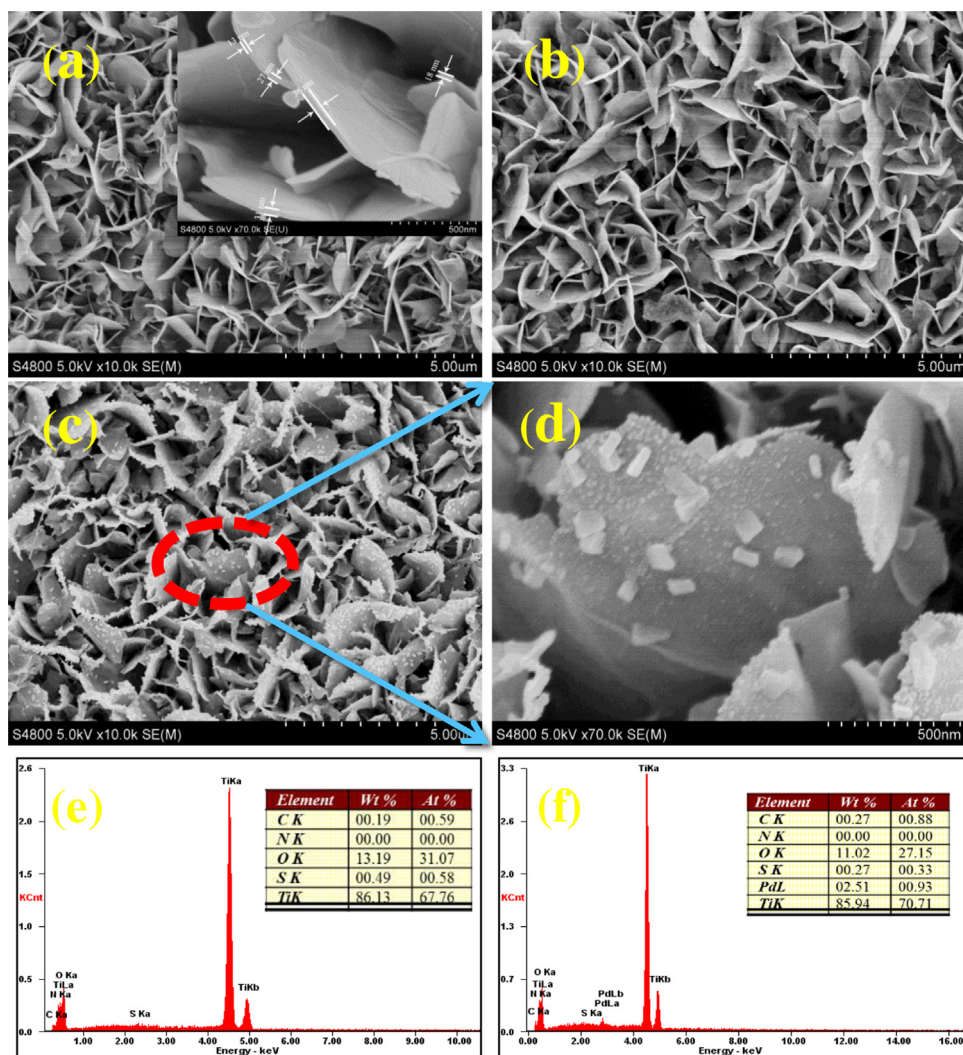
Fig. 1. FE-SEM images of pristine TiO_2 NS (a), C–N–S–TiO_2 NS (b) and Pd/C–N–S–TiO_2 NS (c and d) photoelectrodes, and EDX spectroscopy of C–N–S–TiO_2 NS (e) and Pd/C–N–S–TiO_2 NS (f). (For interpretation of the references to color in the text, the reader is referred to the web version of this article.)

The chemical status of the Pd/C–N–S–TiO_2 NS sample was analyzed by XPS. The corresponding atomic percentage of C, N, S and Pd in the Pd/C–N–S–TiO_2 NS photoelectrode is revealed in Table S1 (Supplementary information). In Fig. 2a, the C1s binding energy peaks were broad and asymmetric, suggesting that there were at least two kinds of C chemical states according to their binding energies ranging from 282 to 291 eV. After fitting of the curve, three peaks at binding energies of 284.6, 286.0 and 288.7 eV were clearly observed, indicating the existence of three different types of C states. The major peak at 284.6 eV could be assigned to adventitious carbon from the XPS instrument itself [32], whereas the other two minor peaks at 286.0 and 288.7 eV could be ascribed to the characteristic of the oxygen bound species C—O and C=O (or O—C—O) bonds [33,34], respectively. The peaks at 286.0 and 288.7 eV could suggest the formation of carbonate species and the substitution of Ti atom by C and formation of Ti-O-C structure, respectively, which can induce the narrowing of the band gap and response to visible light [35,36]. The peak around 282 eV was not observed, implying the absence of substitution of oxygen atom by carbon [37,38]. Meanwhile, Fig. 2b shows the high-resolution XPS spectra of the N of Pd/C–N–S–TiO_2 NS sample. As seen from Fig. 2b, two constituents were found in N1s XPS spectra at around 399.7 and 400.9 eV, which fitted to the XPS data obtained in this work. The main peak at binding energy of 399.7 eV was attributed to the presence of sub-

stitutional nitrogen state as the characteristic of O-Ti-N, indicating that partly lattice oxygen was substituted by N atom [14,33,38]. The other small peak at 400.9 eV could be definitely assigned to interstitial nitrogen atoms as Ti-O-N structural characteristic in the Pd/C–N–S–TiO_2 NS sample [14,33,38]. The S2p XPS peaks centered at 168.6 eV for the Pd/C–N–S–TiO_2 NS sample could be attributed to S^{6+} species as displayed in Fig. 2c, which shifted negatively by 0.4 eV in comparison to the standard binding energy of the sulfur in pure SO_4^{2-} (169.0 eV), could be assigned to the cation S^{6+} in S—O or S=O bonds formed when some of the Ti^{4+} in the TiO_2 lattice were replaced by sulfur atoms [10,33,39]. This was in accordance with the Sano and other group [40,41] that the substitution of Ti^{4+} by S^{6+} is much easier than the replacement of O^{2-} with S^{2-}. The high resolution XPS spectra of the Pd3d region for the Pd/C–N–S–TiO_2 NS sample are presented in Fig. 2d. As shown in Fig. 2d, the emergence of two fitted peaks of Pd at 334.4 and 339.7 eV could be assigned to $Pd°$ $3d_{5/2}$ and $Pd°$ $3d_{3/2}$, respectively, while another two peaks of Pd at 335.7 and 341.6 eV could be ascribed to the Pd^{2+} $3d_{5/2}$ and Pd^{2+} $3d_{3/2}$, respectively [18,25,42]. And the decorated Pd element mainly existed in the form of $Pd°$ according to their peak areas, which indicated that most of the $Pd°$ nanocrystallite was loaded on the surface of TiO_2 nanosheets. Because the cation Pd^{2+} could be transferred to the C–N–S–TiO_2 NS photoanode under the vigorous stirring and then reduced by photoexcited
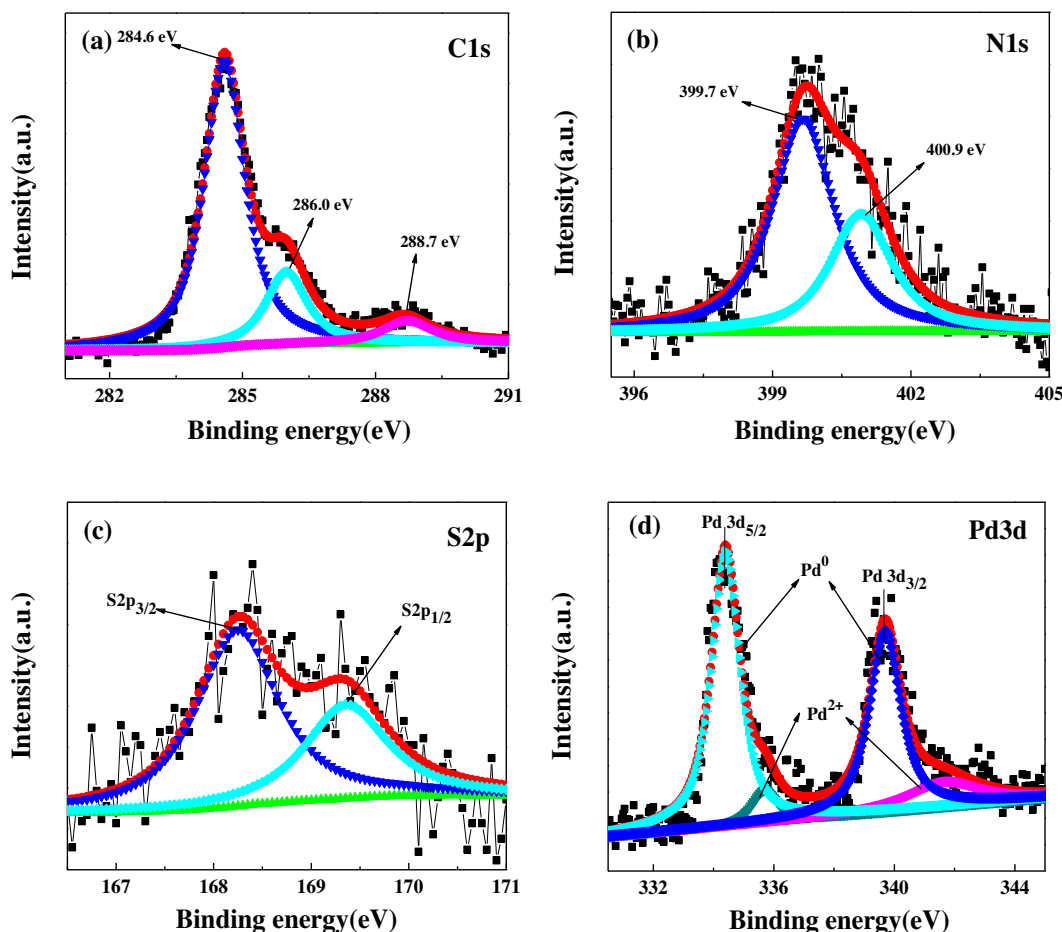
Fig. 2. High-resolution XPS spectra of C1s (a), N1s (b), S2p (c) and Pd3d (d) for the Pd/C-N-S-TiO$_2$ NS photoelectrode.

electrons at the photo-illuminated TiO$_2$ nanosheets/water interface [43]. As demonstrated, the Pd° could promote the migrate of photogenerated electrons from conduction band of TiO$_2$ to the noble metal, consequently increasing the separation of photoinduced charge carriers, further leading to the improvement of PC activity [18]. Moreover, the presence of Pd^{2+} indicated the existence of PdO [25,44].

The crystal structure of the as-prepared pristine TiO$_2$ NS, C-N-S-TiO$_2$ NS and Pd/C-N-S-TiO$_2$ NS samples was revealed by XRD and Raman analysis in Fig. 3. As shown in Fig. 3a, all peaks in the TiO$_2$ NS and C-N-S-TiO$_2$ NS curves could be well-indexed by the anatase (JCPDS NO. 21-1272), rutile phase of TiO$_2$ (JCPDS NO. 21-1276) and the Ti metal phase (JCPDS NO. 44-1294), which were marked distinctly with A, R and T in the XRD patterns, respectively. Compared with pristine TiO$_2$ NS, the intensity of both anatase and rutile diffraction peak of C-N-S-TiO$_2$ NS increased sharply, suggesting the improvement of crystallinity. The XRD pattern of the Pd/C-N-S-TiO$_2$ NS exhibited an additional peaks with 2θ values of 46.5° corresponding to the (200) crystal planes of Pd° nanoparticles, implying the existence of Pd° nano-crystallite [45]. Nevertheless, the diffraction peak of Pd (111) at approximately 2θ = 39.8° was not visible as it might be masked by the Ti substrate peak at 2θ = 40.1°, and the diffraction peak of rutile TiO$_2$ (110) at 2θ = 27.3° could not be seen because of the uniformly dispersed Pd nanoparticles. Furthermore, the peak positions of anatase shifted to lower angles indicated a lattice expansion of TiO$_2$, as the large Pd^{2+} ions (0.080 nm) might replace Ti^{4+} ions (0.064 nm) in TiO$_2$ crystals to generate PdO [25,42], possibly from surface oxidation of Pd° metal by photoexcited holes. Therefore, the XRD results suggested that Pd exists as Pd° nano-

crystallite and PdO in the system, which was consistent with the XPS analysis.

To further verify the crystalline phase of Pd/C-N-S-TiO$_2$ NS, additional Raman spectrum was performed and shown in Fig. 3b. For comparison, the Raman spectra from the TiO$_2$ NS and C-N-S-TiO$_2$ NS were also given. It could be detected that all samples displayed five Raman scattering peaks at around 145.5, 198.1, 396.8, 518.8 and 638.6 cm^{-1}, corresponding to the Raman active modes of anatase with the symmetries of *Eg*, *Eg*, *B1g*, *(A1g + B1g)* and *Eg*, respectively [46]. Interestingly, from the TiO$_2$ NS and C-N-S-TiO$_2$ NS XRD patterns, R (110) diffraction peaks of rutile were detected, but from the corresponding Raman spectra, the Raman features of the rutile phase located at wavenumbers of 235, 448 and 612 cm^{-1} were not observed [47], indicating that all of the samples might only contain a trace of rutile and possessed a main anatase phase composition. In addition, compared with un-doped TiO$_2$ NS, a significant red shift toward high wavenumber region of *Eg* (198.1 cm^{-1}), *B1g* (396.8 cm^{-1}), *(A1g + B1g)* (518.8 cm^{-1}) and *Eg* (638.6 cm^{-1}) bands could be observed for C-N-S-TiO$_2$ NS and the strongest scattering peak of *Eg* (145.5 cm^{-1}) of TiO$_2$ NS became slightly weaker. The shift of the peak positions and the changes of the intensity also suggested that the O or Ti atoms in the lattice of TiO$_2$ were replaced by other elements, namely, C, N and S elements were effectively doped into the lattice of TiO$_2$ NS. After the deposition of Pd nano-crystallite, the Raman scattering peak of C-N-S-TiO$_2$ NS located at 145.5, 198.1, 396.8, 518.8 and 638.6 cm^{-1} became broader and weaker and blue shifted (toward the low wavenumber region) by 0, 2.4, 26.4, 31.1 and 38.3 cm^{-1}, respectively. The blue shift, decrease of the peak intensity and increase in peak broadening demonstrated increas-
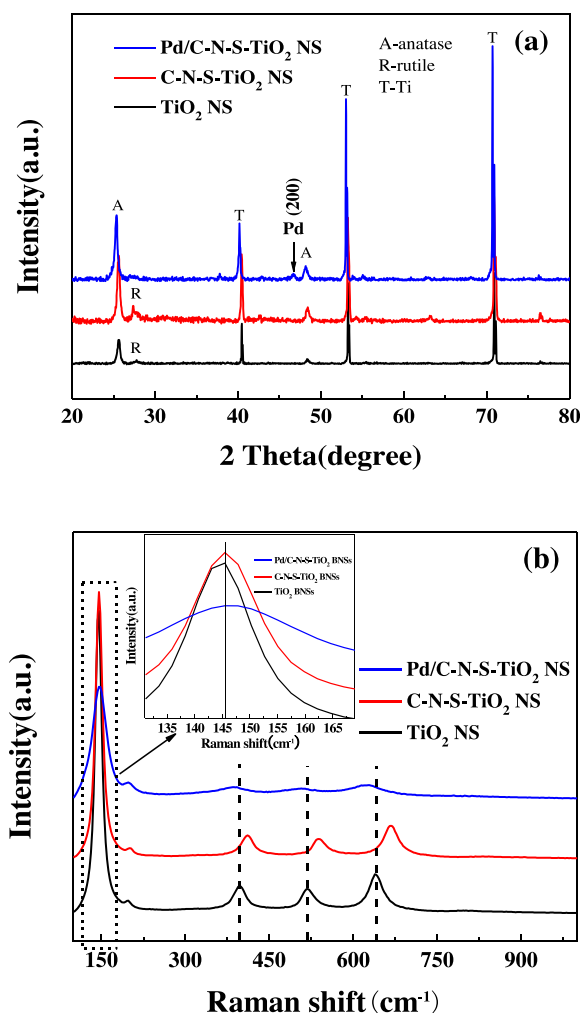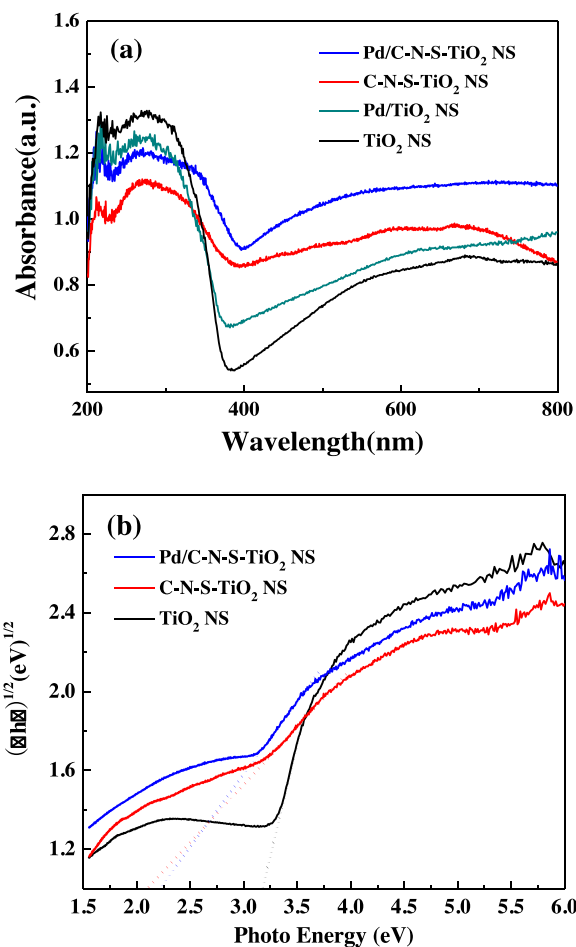
Fig. 3. XRD patterns (a) and Raman spectra (b) of TiO$_2$ NS, C-N-S-TiO$_2$ NS and Pd/C-N-S-TiO$_2$ NS photoelectrodes.

Fig. 4. DRS spectra of as-prepared photoelectrodes (a) and Band gap energy (Eg) of the as-prepared TiO$_2$ NS, C-N-S-TiO$_2$ NS, Pd/C-N-S-TiO$_2$ NS photoelectrodes (b).

ing crystalline defects within the framework of the Pd/C-N-S-TiO$_2$ NS, which might be attributed to the distortion of anatase crystalline lattice induced by the Pd modification [48,49]. These results were correlating well with the characterization of XRD and XPS mentioned above.

3.2. Optical properties

Fig. 4 shows the UV–vis DRS spectra of pristine TiO$_2$ NS, Pd/TiO$_2$ NS, C-N-S-TiO$_2$ NS and Pd/C-N-S-TiO$_2$ NS samples. As displayed in Fig. 4, all of the TiO$_2$ NS samples primarily absorbed the ultraviolet light with wavelengths below 400 nm, corresponding to the intrinsic band gap of TiO$_2$, and also exhibited intense visible light absorption, which was probably caused by the following aspects including the trapped charge carriers or some colored centers, as well as the absorption of incident light by the nanosheets [28], which was consistent with the previous reports. Nevertheless, it could be clearly observed that Pd/TiO$_2$ NS and C-N-S-TiO$_2$ NS all displayed an obvious enhancement of the light absorption in visible light range of 400–800 nm, which was ascribed to that the decorated Pd nano-crystallite could act as sensitizers for capturing a large number of visible-light photons and the co-doping with C, N and S could narrow the band gap of the TiO$_2$ for enlarging the photoresponse into visible-light region, respectively. Further comparison suggested that the Pd/C-N-S-TiO$_2$ NS presented much higher visible absorption intensity than the other TiO$_2$ NS in the

wavelength ranging from 400 to 800 nm. Moreover, the intrinsic absorbance edges of C-N-S-TiO$_2$ NS and Pd/C-N-S-TiO$_2$ NS revealed a remarkable red shift compared to pristine TiO$_2$ NS. The band gap energy could be calculated by employing the Kubelka–Munk formula [50], and the corresponding $(\alpha h\nu)^{1/2}$–$h\nu$ relation curve are shown in Fig. 4b. As roughly calculated, the band gap energies of TiO$_2$ NS, C-N-S-TiO$_2$ NS and Pd/C-N-S-TiO$_2$ NS samples were found to be 3.17 2.08 and 2.20 eV, respectively. This could be chiefly attributed to the synergetic absorption effect of sensitization of deposited Pd nano-crystallite and formation of chemical bonding through co-doping with C, N and S. Specially, the band gap energy of Pd/C-N-S-TiO$_2$ NS was slightly larger than for C-N-S-TiO$_2$ NS sample, which might be due to Pd nano-crystallites on the surface of nanosheets shield some doping sites. The significant enhanced ability of the Pd/C-N-S-TiO$_2$ NS photoelectrode to absorb visible light should make it possessing higher visible light PC activity.

The photoluminescence (PL) emission spectrum, which is a greatly sensitive and non-destructive technique, has always been widely employed in the field of photocatalysis over metal oxides to investigate the electronic structure, optical and photochemical properties of active sites on the surface of semiconductor catalysts [49,51]. From PL spectra, we can obtain information about the surface defects, oxygen vacancies and get surface processes involving charge carrier trapping, transfer and migration, as well as understand the lifetime of photoexcited electron-hole(e$^-$-h$^+$) pairs of photocatalysts since PL emission resulted from the recombination of free charge carriers [51]. Hence, the PL measurements of TiO$_2$ NS, C-N-S-TiO$_2$ NS and Pd/C-N-S-TiO$_2$ NS samples at the
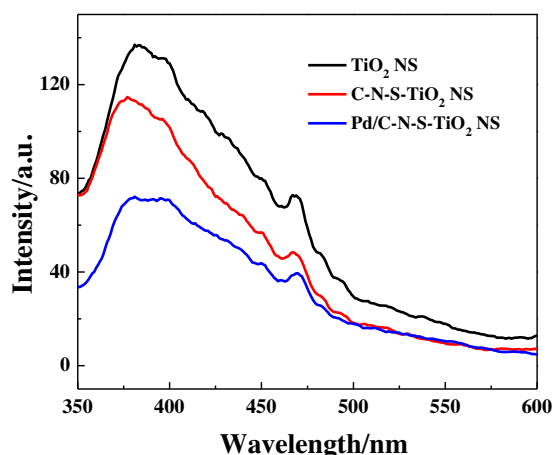
Fig. 5. PL spectra of TiO_2 NS, C-N-S-TiO_2 NS, Pd/C-N-S-TiO_2 NS photoelectrodes.

Fig. 6. SPV spectra of TiO_2 NS, C-N-S-TiO_2 NS, Pd/C-N-S-TiO_2 NS photoelectrodes.

wavelength range from 350 to 600 nm were conducted and displayed in Fig. 5. It was observed that all samples displayed similar PL spectra and strong and wide PL signals in the wavelength between 350 and 425 nm, which was mainly attributed to the band–band PL phenomenon with the energy of light approximately equal to the band gap energy of anatase and rutile [52]. In addition, further observations suggested that emission peaks centered at about 450 (2.76 eV), 468 (2.65 eV), 482 (2.57 eV) and 494 (2.51 eV) nm were assigned to the shallow energy level excitonic PL phenomenon. These excitonic PL emissions were closely associated to the surface states, oxygen vacancies and surface defects [52,53], which could greatly influence PC reactions. Abazovic et al. [54] also indicated that the lower-energy peak of 482 nm (2.57 eV) was induced by the presence of the oxygen vacancies. Generally speaking, lower PL signals may indicate the lower electron-hole recombination rate and the higher separation efficiency, and consequently a longer lifetime of photoinduced charge carriers. Seen from Fig. 5, The PL intensity of TiO_2 NS decreased with the incorporation of the C, N and S elements, indicating that C, N and S co-doping decreased the density of the charge recombination center (such as surface defects and oxygen vacancies) for photoluminescence due to increase the crystallinity of the anatase TiO_2 [55]. And the PL intensity further decreased with the deposition of the Pd nanocrystalline, which revealed that deposition Pd nanocrystalline observably improve the efficiency in charge separation. The Pd nanocrystalline anchored on TiO_2 NS could act as traps to capture the photogenerated electrons from TiO_2, and therefore more effectively restrain the recombination of electrons and holes.

Meanwhile, the photoluminescence quantum yield (f) of the as-prepared TiO_2 NS, C-N-S-TiO_2 NS and Pd/C-N-S-TiO_2 NS samples was contrasted to reflect their charge separation efficiency. It can be defined as the ratio of the number of photons emitted to the number of photons absorbed as follows [49].

f = (Number of photons emitted/Number of photons absorbed) × 100

On the basis of the above results of the UV–vis DRS and PL spectra measurements, the photoluminescence quantum yield of TiO_2 NS, C-N-S-TiO_2 NS and Pd/C-N-S-TiO_2 NS could be semi-quantitatively compared through the peak areas. When the energy of incident light was constant, TiO_2 NS and C-N-S-TiO_2 NS revealed much weaker photons absorption in the wavelength region of 350–600 nm than that of the Pd/C-N-S-TiO_2 NS as shown in Fig. 4. And the photoabsorption intensity of the as-prepared TiO_2 NS samples could be ranged in the following order: Pd/C-N-S-TiO_2 NS > C-N-S-TiO_2 NS > TiO_2 NS. Nevertheless, the larger number of photons (higher PL signals) emitted by the TiO_2 NS than the C-N-
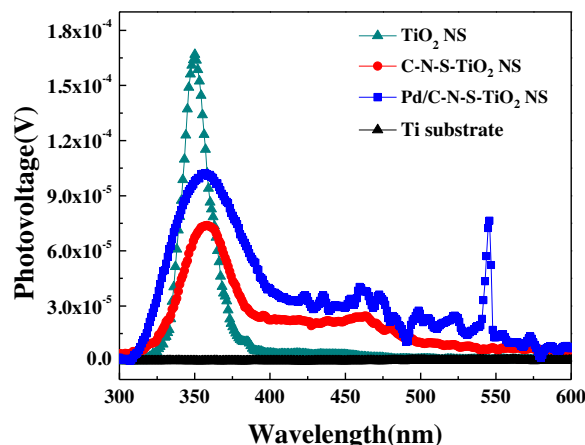
S-TiO_2 NS and Pd/C-N-S-TiO_2 NS could be deduced from Fig. 5. For Pd/C-N-S-TiO_2 NS, it showed lowest number of photons emission (lowest PL signals). This result revealed the photoluminescence quantum yield of the TiO_2 NS and C-N-S-TiO_2 NS are much higher than for Pd/C-N-S-TiO_2 NS. The markedly decreased photoluminescence quantum yield of the TiO_2 NS after the co-doping of C, N and S and loading of Pd nanoparticles also indicated the improved separation of photoinduced electron-hole(e^--h^+) pairs by surface modification.

The surface photovoltage (SPV) is a powerful technique widely used to investigate the surface charge transfer behavior of semiconducting materials. The SPV production primarily derives from the creation of photogenerated electron-hole (e^--h^+) pairs, followed by the separation and transfer upon a built-in electric field [51,56]. Thus, in order to support the aforementioned conclusion, the SPV measurements were carried out to confirm the efficient charge separation of the Pd/C-N-S-TiO_2 NS. Fig. 6 reflects the SPV response of the as-prepared TiO_2 NS, C-N-S-TiO_2 NS and Pd/C-N-S-TiO_2 NS. By comparison, no SPV signals were detected for Ti substrate under the light excitation in the region of 350–600 nm. It could be seen clearly that all samples displayed a distinct SPV response in the UV light regions, which mainly originated from the electronic transitions from the valance band of TiO_2 to its conduction band ($O2p \rightarrow Ti3d$). Additionally, C-N-S-TiO_2 NS exhibited a higher SPV response than pristine TiO_2 NS in the range of 370–600 nm. This phenomenon could be explained principally by the following two reasons. Firstly, the enhancement of crystallization (Fig. 3a) made semiconductor electronic band structure perfect so as to enhance the built-in electric field strength, meanwhile resulting in the decrease in the amount of surface defect and oxygen vacancy, consequently facilitating charge carriers separation and transfer. Secondly, new energy levels were generated in band gap of TiO_2 NS by co-doping with carbon, nitrogen and sulfur, which was favorable to extend optical band gap of TiO_2 [57]. As a result, more visible light could be utilized to create electron-hole (e^--h^+) pairs, leading to a higher concentration separation of visible light excited charge carriers. In addition, it was worth noting that the whole SPV spectra of the C-N-S-TiO_2 NS were distinctly enhanced after the depositing of Pd nano-crystalline, suggesting the higher separation efficiency and the longer lifetime of the charges in comparison with those of TiO_2 NS and C-N-S-TiO_2 NS, which should be attributed to that noble metals Pd nano-crystalline possess a Fermi level lower than TiO_2 semiconductor and could serve as efficient electron acceptors to collect free electron from the semiconductors, therefore inhibiting electron-hole recombination [58]. Besides, another important detail was that the Pd/C-N-S-TiO_2 NS electrodes demonstrated a significantly enhanced SPV signals at around 545 nm, this could
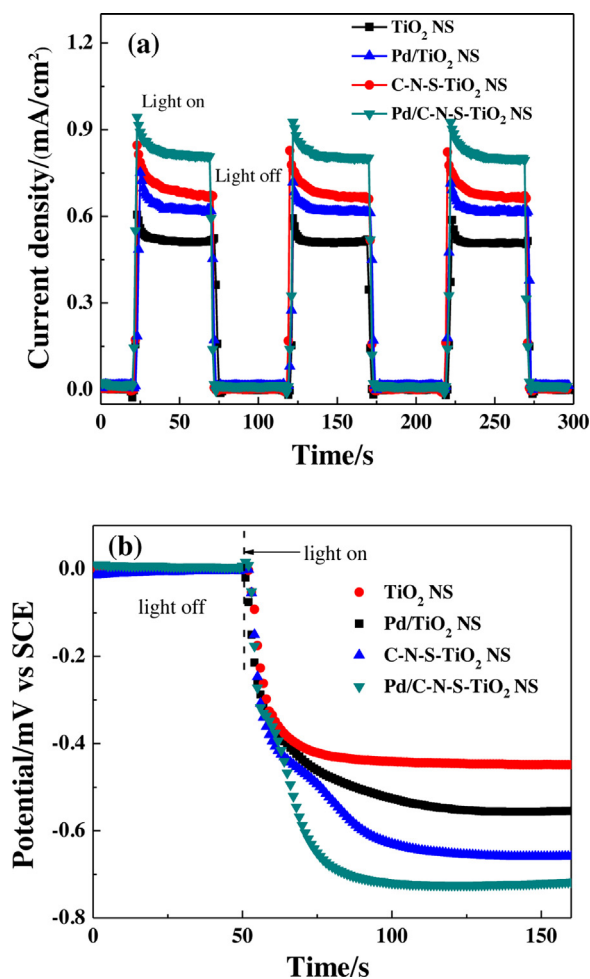
Fig. 7. Transient photocurrent response (a) and open circuit potential (b) of TiO₂ NS, C-N-S-TiO₂ NS, Pd/C-N-S-TiO₂ NS photoelectrodes.

also be thanks to the Pd nanoparticles, which might be associated with the d–d transitions in the Pd nano-crystallite [59]. The SPV responses were in good agreement with the above analysis. Thus, an enhanced PECH and PEC performances of the Pd/C-N-S-TiO₂ NS could be expected.

3.3. PECH performances

Transient photocurrent response and open circuit potential have been demonstrated as the powerful techniques to investigate the separation efficiency of photogenerated electrons and holes at contact semiconductor/electrolyte interfaces in the PC and PEC reaction on TiO₂ photoelectrodes. Thus, transient photocurrent response of the as-prepared TiO₂ NS, Pd/TiO₂ NS, C-N-S-TiO₂ NS and Pd/C-N-S-TiO₂ NS was measured via several on-off cycles under Xenon lamp irradiation as shown in Fig. 7a. Obviously, the photocurrent went down to zero as soon as the irradiation of light on the photoelectrode was stopped, while subsequently shifted to original value as soon as light was switched on again, and all the TiO₂ NS photoanodes displayed good reproducibility and stability under several on-off cycles of intermittent irradiation. Furthermore, it was notable that Pd/C-N-S-TiO₂ NS electrode performed the strongest transient photoresponse with a photocurrent density of 0.806 mA cm⁻², which was larger than that of C-N-S-TiO₂ NS (0.692 mA cm⁻²), Pd/TiO₂ NS (0.614 mA cm⁻²) and pristine TiO₂ NS (0.509 mA cm⁻²) by a factor of 1.16, 1.31 and 1.58, respectively, suggesting that the Schottky junctions formed between TiO₂

NS and Pd nano-crystallite [18] and adulteration with C, N and S elements could significantly improve the separation efficiency of photogenerated charge carriers. As exhibited in Fig. 7b, all the TiO₂ NS photoelectrodes revealed a distinct open circuit potential. Noticeably, Pd/C-N-S-TiO₂ NS performed a higher photovoltage than for C-N-S-TiO₂ NS, Pd/TiO₂ NS and pristine TiO₂ NS. When the Xenon light was switched on, the open circuit potential of Pd/C-N-S-TiO₂ NS shifted gradually and reached to −0.717 mV cm⁻², while the open circuit potential of C-N-S-TiO₂ NS, Pd/TiO₂ NS and TiO₂ NS increased slowly to −0.655 mV cm⁻², −0.554 mV cm⁻² and −0.447 mV cm⁻². Therefore, it could be implied that Pd/C-N-S-TiO₂ NS electrodes displayed a more sensitive and effective separation of photoinduced charge carriers, which was in accordance with the results of photocurrent.

Electrochemical impedance spectroscopy (EIS) has been demonstrated as an effective technique to investigate the electron transport resistance at contact interfaces between TiO₂ photoelectrode and electrolyte in the PC and PEC reactions [60]. Hence, typical EIS Nyquist plots of the TiO₂ NS, Pd/TiO₂ NS, C-N-S-TiO₂ NS and Pd/C-N-S-TiO₂ NS photoelectrodes were recorded under dark and Xenon lamp irradiation. Clearly, as revealed in Fig. 8a, it could be observed that the diameter of the semicircle on the EIS Nyquist plot of the Pd/C-N-S-TiO₂ NS photoelectrode was smaller than that of C-N-S-TiO₂ NS, Pd/TiO₂ NS and TiO₂ NS in the dark. This signified that the charge transfer resistance decreased after the incorporation of C, N and S elements and the deposition of Pd nanoparticles. The decrease in resistance demonstrated that the one-step hydrothermal co-doping and photo-deposition technique used here gave rise to a good interaction of the C, N and S elements and Pd nanocrystalline with the TiO₂ NS, and consequently resulted in an efficient and faster charge transfer path from the Pd/C-N-S-TiO₂ NS to the Ti substrate. Under Xenon lamp irradiation, the diameter of the semicircle on the EIS Nyquist plot of the Pd/C-N-S-TiO₂ NS photoelectrode was lower than that of C-N-S-TiO₂ NS, Pd/TiO₂ NS and TiO₂ NS, which could be attributed to effective separation of photoinduced electron-hole pairs and fast interfacial charge transfer to the electron donor/electron acceptor after TiO₂ NS was modified by C, N and S elements and Pd nanocrystalline under Xenon lamp irradiation (Fig. 8b).

Moreover, as demonstrated, applied external potentials could alter the band bending of nano-materials, which was critical to the separation of photoinduced charge carriers. Thus, Mott–Schottky plots were conducted at room temperature with a frequency of 1000 Hz according to the following equation [61,62]:

$$\frac{1}{C^2} = \frac{2}{N_D e \varepsilon \varepsilon_0} \left(E - E_{FB} - \frac{kT}{e} \right) \tag{1}$$

where C is the space charge capacitance in the semiconductor, T is the temperature, k is the Boltzmann constant, ε is the relative permitivity of the semiconductor, ε_0 is the permittivity of a vacuum, e is the elemental charge, N_D is the charge carrier concentration in a semiconductor, E is the applied potential, and E_{FB} is the flat band potential. Fig. 8c displays the Mott–Schottky plots of $1/C^2$ as a function of the applied potential, from which all the TiO₂ NS photoelectrodes showed positive slopes, suggesting n-type semiconductors. Furthermore, the plots were extrapolated to $1/C^2 = 0$ to estimate the values of E_{FB} (Eq. (1)). As estimated, E_{FB} values for TiO₂ NS, C-N-S-TiO₂ NS and Pd/C-N-S-TiO₂ NS were −0.553, −0.437 and −0.261 V, respectively. Notably, compared to TiO₂ NS and C-N-S-TiO₂ NS, a positive shift of E_{FB} in Pd/C-N-S-TiO₂ NS demonstrated a decrease in bending of the band edge, thereby facilitating the elec-
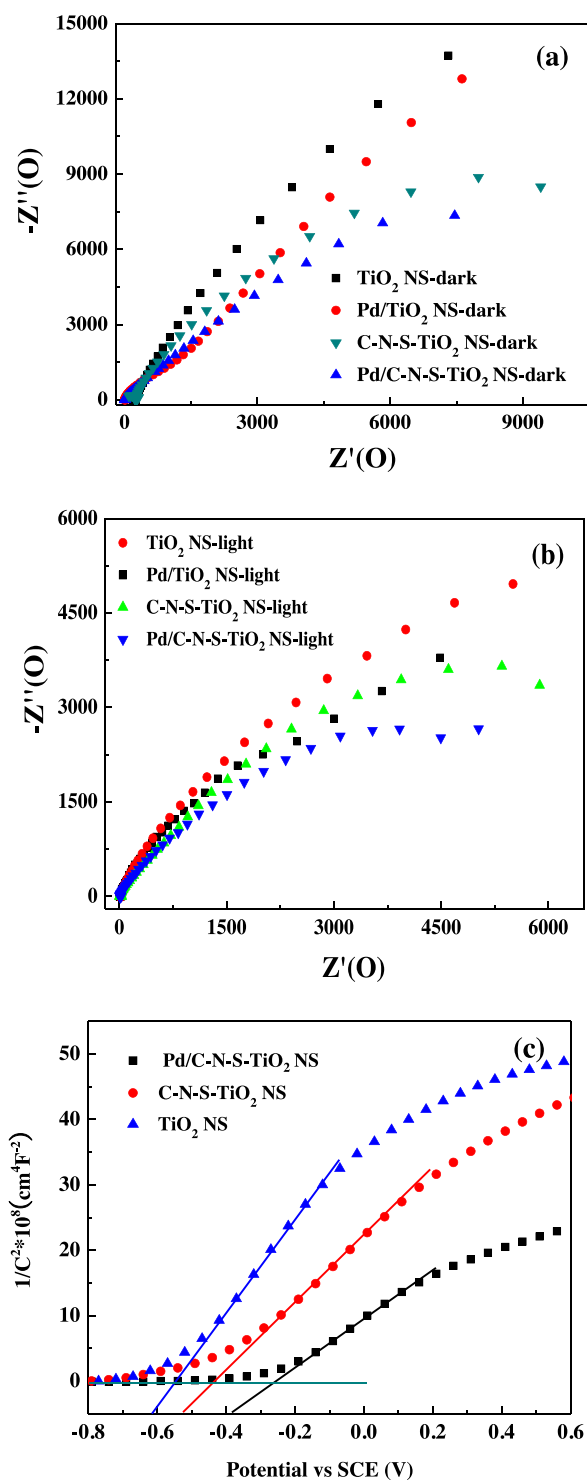
Fig. 8. EIS Nyquist plots of as-prepared photoelectrodes measured at open circuit potential in the dark (a) and under Xenon light irradiation (b); Mott-Schottky plots of TiO₂ NS, C-N-S-TiO₂ NS, Pd/C-N-S-TiO₂ NS photoelectrodes (c).

tron transfer. In addition, the charge carrier density N_D could also be calculated from Fig. 8c using the following equation:

$$N_D = \frac{2}{e\varepsilon\varepsilon_0}\left(\frac{dE}{d\left(\frac{1}{C^2}\right)}\right) \qquad (2)$$

As $e = 1.6 \times 10^{-19}$ C, $\varepsilon_0 = 8.86 \times 10^{-14}$ F/cm, and $\varepsilon = 80$ for TiO₂ [63], the N_D values of TiO₂ NS, C-N-S-TiO₂ NS and Pd/C-N-S-TiO₂ NS

were calculated to be 25×10^{-19}, 34×10^{-19} and 48×10^{-19} cm^{-3}, respectively. Consequently, the higher N_D of Pd/C-N-S-TiO₂ NS indicated a faster carrier transfer than that in TiO₂ NS and C-N-S-TiO₂ NS, and thus an enhanced PC and PEC performance.

3.4. PEC activity and stability

The EC, PC, and PEC experiments for degrading acetylsalicylic acid in aqueous solution were performed on the pristine TiO₂ NS, C-N-S-TiO₂ NS and Pd/C-N-S-TiO₂ NS photoelectrodes under Xenon lamp irradiation. As shown in Fig. 9a, only approximately 6% removal rate of acetylsalicylic acid could be observed by using the EC process for all electrodes, which suggested that the applied external potential on the working electrodes could produce very little oxidative radicals on the electrode surface required for oxidizing acetylsalicylic acid molecules, and co-doping with C, N and S and deposition with Pd nanoparticles did not affect the EC reaction. Notably, much higher degradation of acetylsalicylic acid was obtained during the PC and PEC processes and the degradation efficiency of acetylsalicylic acid could be improved by C, N and S co-doping and Pd nano-crystallite decoration, which was consistent with the optical and PECH results. In addition, the PC and PEC removal efficiencies of the as-prepared TiO₂ NS, C-N-S-TiO₂ NS and Pd/C-N-S-TiO₂ NS electrodes could be ranged in the following order: Pd/C-N-S-TiO₂ NS-PEC > C-N-S-TiO₂ NS-PEC > Pd/C-N-S-TiO₂ NS-PC > TiO₂ NS-PEC > C-N-S-TiO₂ NS-PC > TiO₂ NS-PC. Namely, Pd/C-N-S-TiO₂ NS photoelectrode showed the highest PC and PEC activities, for which 70.8% and 89.1% of acetylsalicylic acid could be degraded after 120 min, respectively, which was mainly attributed to following aspects: (a) adulteration with C, N and S greatly improved the light absorbance in visible region; (b) deposition with Pd nano-crystallite prolonged lifetime and improved separation of photogenerated charge carries; (c) applied potential favored the transfer of photogenerated electrons from working electrode to the cathode, consequently further decreasing the recombination of photogenerated charges. Furthermore, the experimental data of Fig. 9a were found to fit approximately a pseudo-first-order kinetics formula ($-\ln(C/C_0) = kt$) according to the Langmuir–Hinshelwood model [2], as shown in Fig. 9b. Meanwhile, the corresponding pseudo-first-order rate constant (k) was displayed in the inset of Fig. 9b. The rate constants (k) over TiO₂ NS-PC, C-N-S-TiO₂ NS-PC and Pd/C-N-S-TiO₂ NS-PC were 0.0046, 0.0074 and 0.0101 min^{-1}, respectively, while for TiO₂ NS-PEC, C-N-S-TiO₂ NS-PEC and Pd/C-N-S-TiO₂ NS-PEC, the rate constants were 0.0080, 0.0119 and 0.0182 min^{-1}, respectively. The experimental results showed that the reaction rate of acetylsalicylic acid degradation in the PEC using the Pd/C-N-S-TiO₂ NS electrode was the fastest among all the reactions.

Moreover, the visible light PC activities of the as-prepared NS electrodes for degradation of acetylsalicylic acid were also measured as shown in Fig. 9c. Acetylsalicylic acid (<3%) could only be slightly degraded through either direct visible light photolysis without photoelectrodes or adsorption in the dark. For a comparison, the plots of acetylsalicylic acid degradation using TiO₂ NS, Pd/TiO₂ NS, C-N-S-TiO₂ NS and Pd/C-N-S-TiO₂ NS electrodes were included. TiO₂ NS could degrade 15.3% of the acetylsalicylic acid after 120 min of visible light irradiation due to this poor visible light absorption capability shown in the DRS tests and numerous electron traps related to shallow levels (such as oxygen vacancies, surface defects, surface states and trapped states) in the lattice of TiO₂ [24,53,64,65], which was in accordance with the results of PL. These electron traps could capture a small amount of electrons excited by visible light, which the excited energy was less than the band gap energy (3.17 eV) of TiO₂ [52,54,64,66], contributing to the visible light photocatalytic activity. But the majority of electrons on
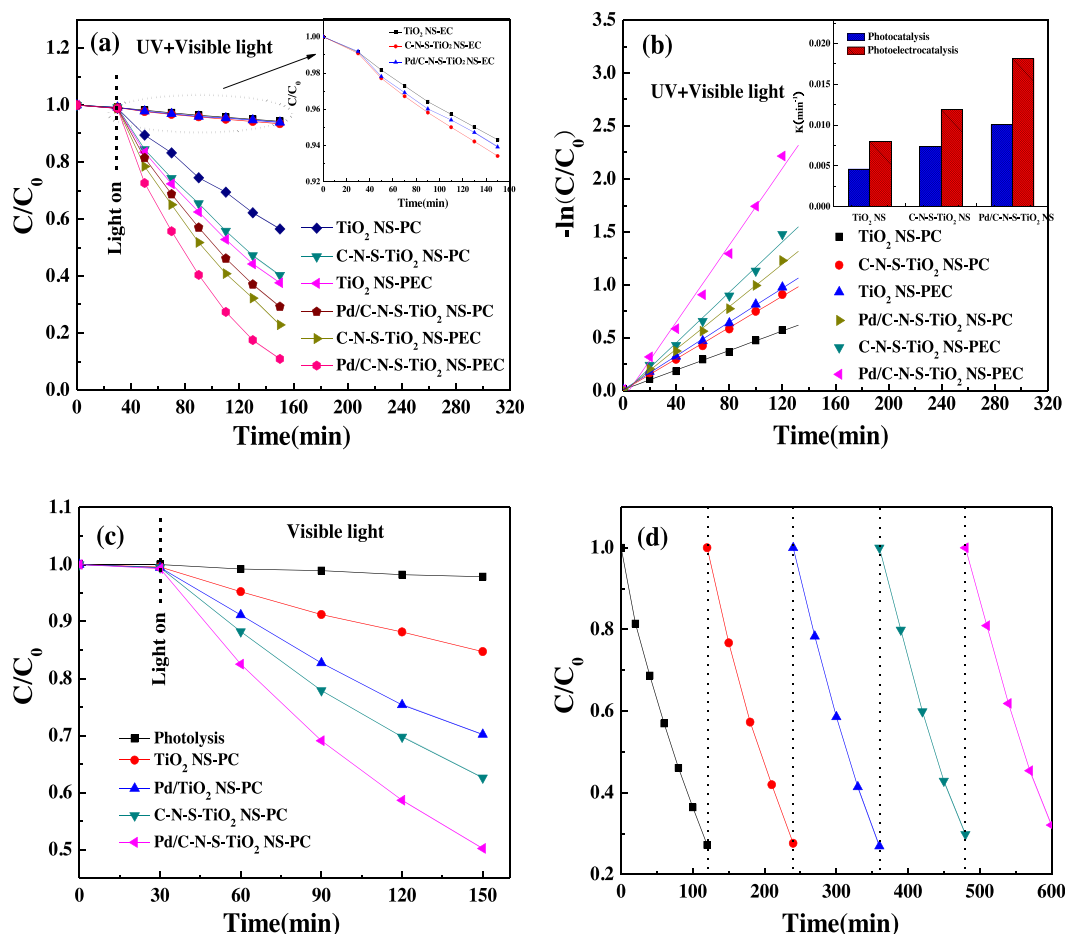
Fig. 9. PC and PEC activities (a) and corresponding dependence of ln(C/C$_0$) on irradiation time (b) towards the degradation of acetylsalicylic acid using TiO$_2$ NS, C-N-S-TiO$_2$ NS, Pd/C-N-S-TiO$_2$ NS photoelectrodes under Xenon light irradiation (Inset in b showed the comparison of the constant rate of various photoelectrodes in PC and PEC reactions.); the PC activity of the as-prepared photoelectrodes under visible light (λ > 420 nm) irradiation (c); repeated utilization of the as-obtained Pd/C-N-S-TiO$_2$ NS photoelectrode (d).

the valence band of TiO$_2$ could not be excited and transferred to its conduction band under visible light illumination, thereby showing a low visible light photocatalytic activity. The visible PC activity of TiO$_2$ NS was obviously improved after modifying with Pd nanocrystallite or cystine. The degradation efficiency using Pd/TiO$_2$ NS and C-N-S-TiO$_2$ NS were 29.8% and 37.4% after 120 min, respectively. When cystine and Pd nano-crystallite were both modified on the TiO$_2$ NS, the visible PC activity further greatly increased and attained 49.8% within 120 min. This could be ascribed to the formation of the doped species and the Schottky junctions. Hence, it was confirmed that the resulting Pd/C-N-S-TiO$_2$ NS photoelectrode could exhibit good visible light PC performance for degradation of pollutant. The stability and recyclability of the obtained Pd/C-N-S-TiO$_2$ NS photoelectrode was also investigated. As shown in Fig. 9d, no apparent decrease of PC activity was observed after five consecutive runs under Xenon light irradiation, indicating the excellent PC stability of the photoelectrode for the treatment of organic contaminants in wastewater.

3.5. Free radicals scavenging experiments and mechanism analysis

With the purpose of understanding the PC mechanism of Pd/C-N-S-TiO$_2$ NS photoelectrode for pollutant degradation, the active species including h$^+$, H$_2$O$_2$, •O^{2-} radicals and •OH radicals, which were responsible for the decomposition of pollutants, produced during the process of photoelectrode-photocatalyzed acetylsali-

cylic acid removal were detected through free radicals scavenging experiments. Fig. 10a reveals the effect of various scavengers on the PC activities of Pd/C-N-S-TiO$_2$ NS electrode towards the degradation of acetylsalicylic acid. Noticeably, the PC efficiency of Pd/C-N-S-TiO$_2$ NS was 70.8% after 120 min of Xenon lamp irradiation without scavenger. As a kind of scavenger for •OH radicals [67], the addition of 10 mmol t-BuOH could decrease the PC activity to the largest extent (from 70.8% to 13.1%), implying that •OH radicals was the dominated active species for the photodegradation process in current system. Benzoquinone (BQ) was employed to trap •O^{2-} radicals [68]. After the addition of 10 mmol BQ, the PC degradation of acetylsalicylic acid was significantly decreased (from 70.8% to 30.7%), which meant •O^{2-} radicals also played an important role in our PC process. When ammonium oxalate (AO) as a scavenger for h$^+$ species was added into the PC system [69], the degradation rate of acetylsalicylic acid was moderately inhibited (from 70.8% to 51.5%). On the other words, h$^+$ had the minor contribution for the pollutant removal. In addition, Fe(II)-EDTA was employed to investigate the role of H$_2$O$_2$ during the PC reaction [70]. It can be observed that the PC degradation of acetylsalicylic acid was partial suppressed (from 70.8% to 44.7%), suggesting that the role of H$_2$O$_2$ was slightly higher than that of h$^+$ in our PC system. Furthermore, it is well known that O$_2$ as an electron scavenger can capture photogenerated electrons to produce various kinds of reactive oxygen species [71]. Consequently the PC activity could be inhibited under anaerobic conditions. O$_2$ or N$_2$ bubbles into the PC reaction system could be utilized to investigate the influence of dis-
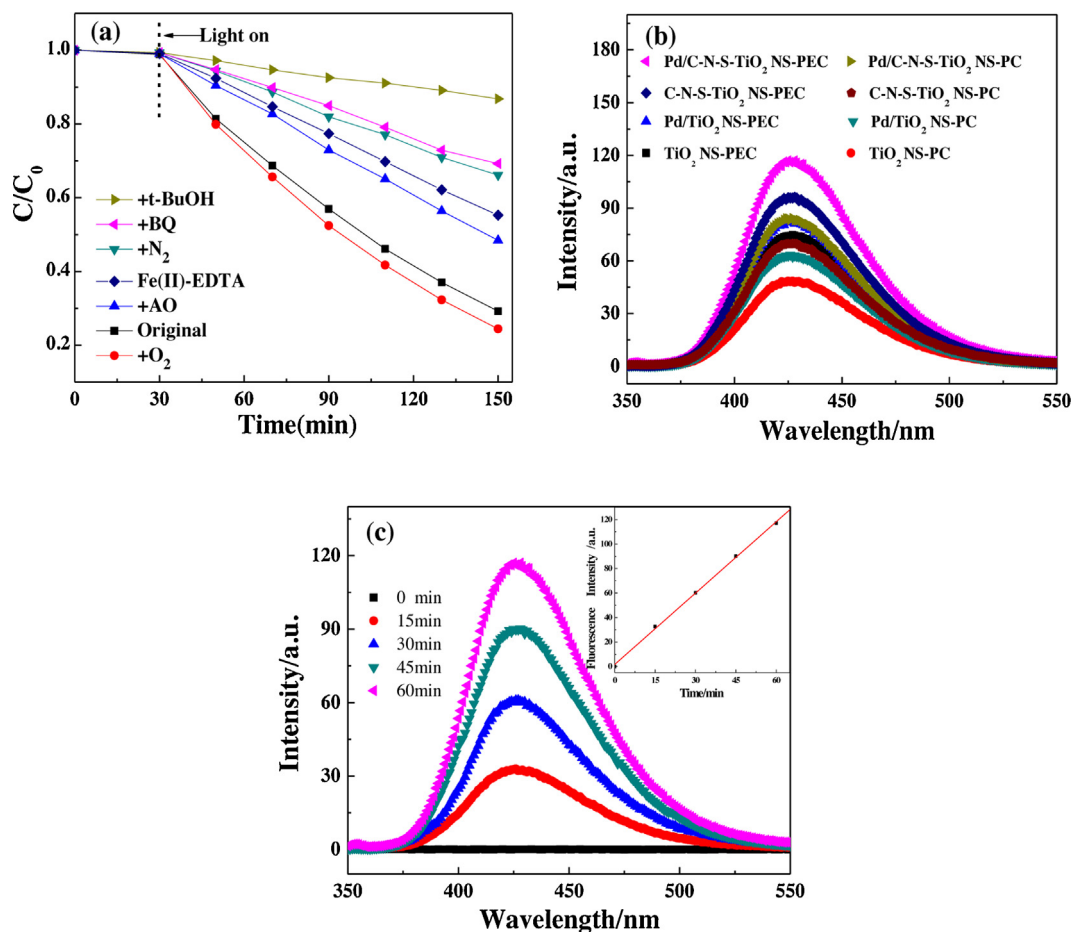
Fig. 10. Effect of various scavengers on the PC activity of Pd/C-N-S-TiO$_2$ NS photoelectrode for degrading acetylsalicylic acid (a); FL spectra changes at a fixed 60 min on as-prepared photoelectrodes in 0.0005 mol L^{-1} TA solution with or without 2 V external potentials (b). FL spectra with Xenon lamp irradiation time using Pd/C-N-S-TiO$_2$ NS photoelectrodes (c).
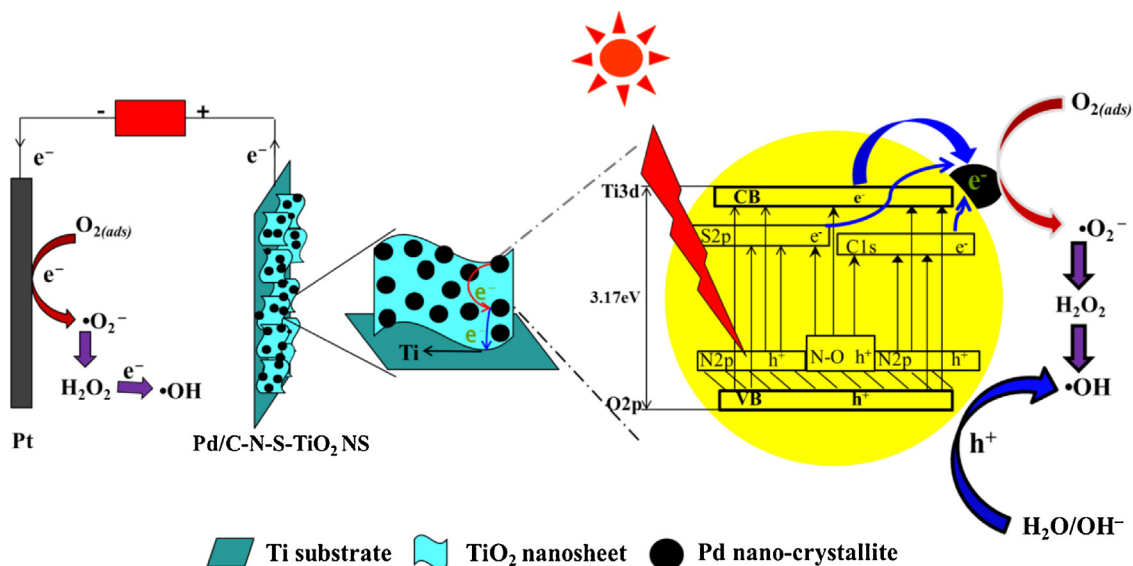
Fig. 11. Schematic diagram of the charge transfer for PC and PEC reaction on Pd/C-N-S-TiO$_2$ NS photoelectrode.

solved O$_2$ during the PC process. As a result, when bubbled with N$_2$ constantly, O$_2$ molecules could be thoroughly discharged from the reaction system, preventing the generation of •O$_2^-$, H$_2$O$_2$ and •OH, the PC activity decreased greatly (33.8%). Nevertheless, it could be observed that the PC degradation efficiency of acetylsalicylic acid

enhanced slightly upon being bubbled with O$_2$ continually (75.6%). Hence, according to the analysis of the above results, we could conclude that the PC performance of Pd/C-N-S-TiO$_2$ NS for degrading acetylsalicylic acid was partly ascribed to the active species (•O^{2-} and •OH) generated from the reaction between the photoin-

duced electrons from TiO_2 NS and dissolved O_2. And degradation of acetylsalicylic acid was mainly achieved by the participation of •OH radicals. •O^{2-} radicals were a sub-mainly active species, while H_2O_2 and h^+ contributed a less extent.

The formation of •OH radicals were further detected through terephthalic acid fluorescence (FL) probing technique. This approach was based on an effortless reaction of •OH radicals with terephthalic acid (TA) to form highly fluorescent product, 2-hydroxyterephthalic acid (TAOH) with a characteristic fluorescence at about 425 nm [72]. Fig. 10b displays the comparative FL intensity of TAOH at a fixed 60 min in the presence of as-prepared pristine TiO_2 NS, Pd/TiO_2 NS, C-N-S-TiO_2 NS and Pd/C-N-S-TiO_2 NS electrodes under Xenon lamp irradiation with or without 2 V external applied potentials. Obviously, FL intensity of the produced TAOH at the surface of Pd/C-N-S-TiO_2 NS was stronger than that of other electrodes with or without external potential, indicating that Pd/C-N-S-TiO_2 NS should possess largest amount of •OH radicals. Besides, when 2 V external potential was applied, the FL intensity of TAOH at 425 nm of all electrodes greatly increased. The evolution of FL intensity of TAOH followed the same tendency with the PC and PEC (in Fig. 9a) performance. This manifested that Pd/C-N-S-TiO_2 NS electrode could generate more •OH radicals to participate in the catalytic reaction, thereby leading to a higher PC and PEC activity. Fig. 10c exhibits the changes of FL intensity of TAOH as a function of continuous Xenon light irradiation on the Pd/C-N-S-TiO_2 NS electrode. Noticeably, the intensity of the FL peak at 425 nm increased steadily with prolonging irradiation time. Interestingly, the FL intensity increased linearly as the illumination time (as shown in the inset of Fig. 10c), indicating that the amount of •OH radicals generated on the surface of Pd/C-N-S-TiO_2 NS was proportional to the Xenon lamp illumination time. Nevertheless, no TAOH peak was detected in the absence of the illumination of Pd/C-N-S-TiO_2 NS electrode.

Based on the above systematic analysis, a reasonable PC and PEC mechanism for the degradation of acetylsalicylic acid process using Pd/C-N-S-TiO_2 NS as the photoanode was proposed and illustrated in Fig. 11. In PC process, the carbonate species and doped S species created additional two impurity levels by replacing Ti^{4+} below the conduction band of TiO_2, and the doped N species also generated a new impurity level above the valence band of TiO_2 [7,9,13,39,41,73], which could be aroused by visible light to produce charge carriers. The specific energy level position of doped C, N and S we decided in this case referred to our previous study [33]. After depositing Pd nano-crystallite, a Schottky junction was formed at Pd/TiO_2 NS interfaces owing to the large work function of palladium, therefore photogenerated electrons (e^-) could easily transfer from conduction band of Pd/C-N-S-TiO_2 NS into Pd nano-crystallite, remaining highly oxidative holes (h^+) on the valence band. Afterwards, the separated photogenerated electrons would reduce the absorbed O_2 to produce •O^{2-} radicals. Following a series of reactions with H_2O and e^-, the active •O^{2-} radicals further formed H_2O_2 and •OH radicals, which might come from the reactions of •$O^{2-} + 2H^+ \rightarrow H_2O_2$ and $H_2O_2 + e^- \rightarrow •OH + OH^-$ [71,74]. And photogenerated holes on the valence band would easily react with the H_2O molecules to generate •OH radicals. Eventually, acetylsalicylic acid molecules were decomposed by those active species (h^+, H_2O_2, •O^{2-} radicals and •OH radicals). In PEC process, with the assistance of external applied potential between photoanode (Pd/C-N-S-TiO_2 NS electrode) and cathode (Pt electrode), the electrons could transfer along the TiO_2 nanosheets arrays to the Ti substrate and finally reach the cathode via outer circuit. At such, more effectively charge carriers separation would be achieved, leading to longer lifetime of the photoinduced charge carriers. Subsequently, the separated charge carriers could effectively take part in the formation of active

oxygen species (H_2O_2, •O^{2-} and •OH radicals) and consequently further improved PC performance.

4. Conclusions

In summary, we had successfully prepared a visible light active Pd/C-N-S-TiO_2 NS photoelectrode via a hydrothermal method, followed by photo-assisted deposition strategy. Series of characterization indicated that a small amount of carbon, nitrogen and sulfur were co-doped into the lattice of TiO_2 and Pd nanocrystallite existed mainly in the form of Pd°, which induced an excellent absorption capacity in the visible light region. In addition, Pd/C-N-S-TiO_2 NS electrode possessed higher photovoltage, photocurrent density and charge carrier density. Compared with the others TiO_2 NS, the enhanced PC and PEC activity of the Pd/C-N-S-TiO_2 NS towards the removal of acetylsalicylic acid and generation of •OH radicals were obtained and explained by the effective separation and transportation of the photogenerated charge carriers as well as the strong visible light absorption. The as-obtained Pd/C-N-S-TiO_2 NS photoelectrode displayed enough catalytic stability as evidenced through the recycling experiments. Furthermore, it could be concluded that •OH radicals was the dominant active species in PC process. This work not only indicated that Pd/C-N-S-TiO_2 NS electrode was highly suitable as a visible light driven photocatalyst for the degradation of hazardous pollutants, but also might provide helpful information towards the future design and practical application of multifunctional hybrids photoelectrodes applied in the field of environment remediation and energy conversion.

Acknowledgments

Appendix A. Supplementary data

Supplementary data associated with this article can be found, in the online version, at http://dx.doi.org/10.1016/j.apcatb.2016.02.019.

References

[1] F. Lin, D. Wang, Z.X. Jiang, Y. Ma, J. Li, R.G. Li, C. Li, Energy Environ. Sci. 5 (2012) 6400–6406.
[2] M.R. Hoffman, S.T. Martin, W.Y. Chio, D.W. Bahnemann, Chem. Rev. 95 (1995) 69–96.
[3] N. Zhang, M.Q. Yang, S. Liu, Y. Sun, Y.J. Xu, Chem. Rev. 115 (2015) 10307–10377.
[4] M.Y. Wang, J. Ioccozia, L. Sun, C.J. Lin, Z.Q. Lin, Energy Environ. Sci. 7 (2014) 2182–2202.
[5] Z.F. Jiang, D.L. Jiang, Z.X. Yan, D. Liu, K. Qian, J.M. Xie, Appl. Catal. B: Environ. 170–171 (2015) 195–205.
[6] Q.H. Chen, H.L. Liu, Y.J. Xin, X.W. Cheng, Chem. Eng. J. 241 (2014) 145–154.
[7] R. Asahi, T. Morikawa, T. Ohwaki, K. Aoki, Y. Taga, Science 293 (2001) 269–271.
[8] T.C. Jagadale, S.P. Takale, R.S. Sonawane, H.M. Joshi, S.I. Patil, B.B. Kale, S.B. Ogale, J Phys. Chem. C 112 (2008) 14595.
[9] J.L. Jia, D. Li, J.F. Wan, X.J. Yu, J. Ind. Eng. Chem. 33 (2016) 162–169.
[10] D. Ma, Y.J. Xin, M.C. Gao, J. Wu, Appl. Catal. B: Environ. 147 (2014) 49–57.
[11] G.G. Bessegato, J.C. Cardoso, M.V.B. Zanoni, Catal. Today 240 (2015) 100–106.
[12] W. Yu, X.J. Liu, L.K. Pan, J.L. Li, J.Y. Liu, J. Zhang, P. Li, C. Chen, Z. Sun, Appl. Surf. Sci. 319 (2014) 107–112.
[13] L. Sun, J.H. Cai, Q. Wu, P. Huang, Y.F. Su, C.J. Lin, Electrochim. Acta 108 (2013) 525–531.
[14] G.S. Zhang, Y.C. Zhang, M. Nadagouda, C. Han, K. O'shea, S.M. El-Sheikh, A.A. Ismail, D.D. Dionysiou, Appl. Catal. B: Environ. 144 (2014) 614–621.
[15] E.M. Samsudin, S.B.A. Hamid, J.C. Juan, W.J. Basirun, G. Centi, Chem. Eng. J. 280 (2015) 330–343.

[16] V. Trevisan, A. Olivo, F. Pinna, M. Signoretto, F. Vindigni, G. Cerrato, C.L. Bianchi, Appl. Catal. B: Environ. 160–161 (2014) 152–160.

[17] L.L. Tan, W.J. Ong, S.P. Chai, A.R. Mohamed, Appl. Catal. B: Environ. 166–167 (2015) 251–259.

[18] X.W. Cheng, H.L. Liu, Q.H. Chen, J.J. Li, P. Wang, J. Hazard. Mater. 254–255 (2013) 141–148.

[19] J.J. Li, H.L. Li, X.W. Cheng, Q.H. Chen, Y.J. Xin, Z.P. Ma, W.X. Xu, J. Ma, N.Q. Ren, Chem. Eng. J. 225 (2013) 489–498.

[20] M.C. Yang, Y.Y. Lee, B. Xu, K. Powers, Y.S. Meng, J. Power Sources 27 (2012) 166–172.

[21] C.H. Wang, X.T. Zhang, Y.L. Zhang, Y. Jia, J.K. Yang, P.P. Sun, Y.C. Liu, J. Phys. Chem. C 115 (2011) 22276–22285.

[22] J.Y. Liao, B.X. Lei, H.Y. Chen, D.B. Kuang, C.Y. Su, Energy Environ. Sci. 5 (2012) 5750–5757.

[23] M. Xi, Y.L. Zhang, L.Z. Long, X.J. Li, J. Solid State Chem. 219 (2014) 118–126.

[24] Q.H. Chen, H.L. Liu, Y.J. Xin, X.W. Cheng, Electrochim. Acta 111 (2013) 284–291.

[25] M.D. Ye, J.J. Gong, Y.K. Lai, C.J. Lin, Z.Q. Lin, J. Am. Chem. Soc. 134 (2012) 15720–15723.

[26] Y. Hou, X.Y. Li, X.J. Zou, X. Quan, G.H. Chen, Environ. Sci. Technol. 43 (2009) 858–863.

[27] D. Li, X.J. Yu, X.W. Cheng, Funct. Mater. Lett. 8 (2015) 1550034.

[28] D. Li, X.W. Cheng, X.J. Yu, Z.P. Xing, Chem. Eng. J. 279 (2015) 994–1003.

[29] L. Ren, Y.Z. Li, J.T. Hou, J.L. Bai, M.Y. Mao, M. Zeng, X.J. Zhao, N. Li, Appl. Catal. B: Environ. 181 (2016) 625–634.

[30] D.Z. Lu, P.F. Fang, X.Z. Liu, S.B. Zhai, C.H. Li, X.N. Zhao, J.Q. Ding, R.Y. Xiong, Appl. Catal. B: Environ. 179 (2015) 558–573.

[31] Z.W. Tong, D. Yang, T.X. Xiao, Y. Tian, Z.Y. Jiang, Chem. Eng. J. 260 (2015) 117–125.

[32] W.J. Ren, Z.H. Ai, F.L. Jia, L.Z. Zhang, X.X. Fan, Z.G. Zou, Appl. Catal. B: Environ. 69 (2007) 138–144.

[33] D. Li, Z.P. Xing, X.J. Yu, X.W. Cheng, Electrochim. Acta 170 (2015) 182–190.

[34] V. Kiran, S. Sampath, ACS Appl. Mater. Interfaces 4 (2012) 3818–3828.

[35] H.Q. Wang, Z.B. Wu, Y. Liu, J. Phys. Chem. C 113 (2009) 13317–13324.

[36] Y. Zhang, Z. Zhao, J. Chen, L. Cheng, J. Chang, W. Sheng, C. Hu, S. Cao, Appl. Catal. B: Environ. 165 (2015) 715–722.

[37] J. Yu, Q. Li, S. Liu, M. Jaroniec, Chem. Eur. J. 19 (2013) 2433–2441.

[38] W. Qian, P.A. Greaney, S. Fowler, S.K. Chiu, A.M. Goforth, J. Jiao, ACS Sustainable Chem. Eng. 2 (2014) 1802–1810.

[39] J.C. Yu, W.K. Ho, J.G. Yu, H.P. Yip, P.K. Wong, J.C. Zhao, Environ. Sci. Technol. 39 (2005) 1175–1179.

[40] T. Ohno, T. Mitsui, M. Matsumura, Chem. Lett. 32 (2003) 364–365.

[41] T. Sano, N. Mera, Y. Kanai, C. Nishimoto, S. Tsutsui, T. Hirakawa, N. Negishi, Appl. Catal. B: Environ. 128 (2012) 77–83.

[42] Y. Chang, J. Xu, Y. Zhang, S. Ma, L. Xin, L. Zhu, C. Xu, J. Phys. Chem. C 113 (2009) 18761–18767.

[43] K. Mori, T. Araki, T. Takasaki, S. Shironita, H. Yamashita, Photochem. Photobiol. Sci. 8 (2009) 652–656.

[44] O.V. Safonova, M.N. Rumyantseva, R.I. Kozlov, M. Labeau, G. Delabouglise, L.I. Ryabova, A.M. Gaskov, Mater. Sci. Eng. B 77 (2000) 159–166.

[45] M.L. Zhang, T. Ning, S.Y. Zhang, Z.M. Li, Z.H. Yuan, Q.X. Cao, Mater. Sci. Semicond. Process. 17 (2014) 149–154.

[46] D.S. Guan, J.Y. Li, X.F. Gao, C. Yuan, J. Power Sources 246 (2014) 305–312.

[47] Y.J. Xin, H.L. Liu, J.J. Li, Q.H. Chen, D. Ma, J. Solid State Chem. 199 (2013) 49–55.

[48] H.X. Li, Z.F. Bian, J. Zhu, Y.N. Huo, H. Li, Y.F. Lu, J. Am. Chem. Soc. 129 (2007) 4538–4539.

[49] Y. Hou, X.Y. Li, Q.D. Zhao, X. Quan, G.H. Chen, J. Mater. Chem. 21 (2011) 18067–18076.

[50] F. Spadavecchia, C. Cappelletti, S. Ardizzone, C.L. Bianchi, S. Cappelli, C. Oliva, P. Scardi, M. Leoni, P. Fermo, Appl. Catal. B: Environ. 96 (2010) 314–322.

[51] M. Humayun, A. Zada, Z.J. Li, M.Z. Xie, X.L. Zhang, Y. Qu, F. Raziq, L.Q. Jing, Appl. Catal. B: Environ. 180 (2016) 219–226.

[52] L.Q. Jing, X.J. Sun, W.M. Cai, Z.L. Xu, Y.G. Du, H.G. Fu, J. Phys. Chem. Solids 64 (2003) 615–623.

[53] X.W. Cheng, H.L. Liu, Q.H. Chen, J.J. Li, P. Wang, Electrochim. Acta 103 (2013) 134–142.

[54] N.D. Abazovic, M.I. Comor, M.D. Dramicanin, D.J. Jovanovic, S.P. Ahrenkiel, J.M. Nedeljkovic, J. Phys. Chem. B 110 (2006) 25366–25370.

[55] Q.H. Chen, H.L. Liu, Y.J. Xin, X.W. Cheng, Electrochim. Acta 111 (2013) 284–291.

[56] X.W. Cheng, X.J. Yu, Z.P. Xing, Mater. Res. Bull. 47 (2012) 3804–3809.

[57] X.W. Cheng, X.J. Yu, Z.P. Xing, Appl. Surf. Sci. 258 (2012) 3244–3248.

[58] C.G. Silva, R. Juárez, T. Marino, R. Molinari, H. García, J. Am. Chem. Soc. 133 (2011) 595–602.

[59] R. Camposeco, S. Castillo, I. Mejía-Centeno, J. Navarrete, J. Marín, Mater. Charact. 95 (2014) 201–210.

[60] Y. Hou, X.Y. Li, Q.D. Zhao, X. Quan, G.H. Chen, Environ. Sci. Technol. 44 (2010) 5098–5103.

[61] R. O'Hayre, M. Nanu, J. Schoonman, A. Goossens, J. Phys. Chem. C 111 (2007) 4809–4814.

[62] Z. Zhang, Y. Yu, P. Wang, ACS Appl. Mater. Interfaces 4 (2012) 990–996.

[63] M. Mikula, J. Blecha, M. Ceppan, J. Electrochem. Soc. 139 (1992) 3470–3474.

[64] L. Danzhen, Z. Yi, F. Xianzhi, Chin. J. Mater. Res. 14 (2000) 639–642.

[65] R.G. Li, Y.X. Weng, X. Zhou, X.L. Wang, Y. Mi, R.F. Chong, H.X. Han, C. Li, Energy Environ. Sci. 8 (2015) 2377–2382.

[66] X.Y. Pan, M.Q. Yang, X.Z. Fu, N. Zhang, Y.J. Xu, Nanoscale 5 (2013) 3601–3614.

[67] F.T. Li, S.J. Wang, Y. Zhao, J.X. Liu, Y.J. Hao, R.H. Liu, D.S. Zhao, Appl. Catal. B: Environ. 144 (2014) 442–453.

[68] L. Ye, J. Liu, C. Gong, L. Tian, T. Peng, L. Zan, ACS Catal. 2 (2012) 1677–1683.

[69] W.J. Li, D.Z. Li, W.J. Zhang, Y. Hu, Y.H. He, X.Z. Fu, J. Phys. Chem. C 114 (2010) 2154–2159.

[70] Y.M. Chen, A.H. Lu, Y. Li, L.S. Zhang, H.Y. Yip, H.J. Zhao, T.C. An, P.K. Wong, Environ. Sci. Technol. 45 (2011) 5689–5695.

[71] Y. Shao, C.S. Cao, S.L. Chen, M. He, J.L. Fang, J. Chen, X.F. Li, D.Z. Li, Appl. Catal. B: Environ. 179 (2015) 344–351.

[72] K. Ishibashi, A. Fujishima, T. Watanabe, K. Hashimoto, Electrochem. Commun. 2 (2000) 207–210.

[73] H. Kamisaka, T. Adachi, K. Yamashita, J. Chem. Phys. 123 (2005) 084704.

[74] P. Salvador, J. Phys. Chem. C 111 (2007) 17038–17043.